

Analysis of Permanent Magnet Synchronous Generator for Vortex Induced Vibration Hydrokinetic Energy Applications Based on Analytical Magnetic Field Calculations

Jang-Young Choi¹, Hyun-Jae Shin¹, Jong-Su Choi^{2*}, Sup Hong², Tae-Kyeong Yeu², and Hyung-Woo Kim²

¹Department of Electrical Engineering, Chungnam National University, Daejeon 305-764, Korea

²Ocean System Engineering Research Department, Korea Ocean Research & Development Institute, Daejeon 305-343, Korea

(Received 2 December 2011, Received in final form 1 February 2012, Accepted 20 February 2012)

This paper deals with the performance analysis and estimation of the electrical parameters of a permanent magnet synchronous generator (PMSG) for hydrokinetic energy conversion applications using vortex induced vibration (VIV). The analytical solutions for the magnetic fields produced by permanent magnets (PMs) and stator winding currents are obtained using a 2D polar coordinate system and a magnetic vector potential. An analytical expression for the 2D permeance is also derived, which takes into account stator skew effects. Based on these magnetic field solutions and the 2D permeance function, electrical circuit parameters such as the back-emf constant and the air-gap inductance are obtained analytically. The performances of the PMSG are investigated using the estimated electrical circuit parameters and an equivalent circuit (EC). All analytical results are validated extensively using 2D finite element (FE) analyses. Experimental measurements for parameters such as the back-emf and inductance are also presented to confirm the analyses.

Keywords : electrical parameter estimation, permanent magnet synchronous generator, hydrokinetic energy, magnetic fields

1. Introduction

Environmental concerns have spurred research into renewable electrical power sources and hydrokinetic power is one of the most promising sources. Hydrokinetic energy conversion systems are increasingly being considered as attractive alternative solutions for electric power generation from marine or tidal currents, river streams, and other artificial waterways [1]. In particular, there has been a recent increase in research interest on hydrokinetic energy converters using vortex induced vibration (VIV). VIV occurs when the vortex shedding frequency is approximately equal to the structure's natural frequency [2]. When the VIV frequency approaches one of the natural frequencies of the structure, i.e., approaches resonance, lock-in occurs.

In order to extract the maximum electrical energy from the hydrokinetic energy converter using VIV, first of all, the performance of the overall system should be investigated. To do this, an analysis of the characteristics of each element in the system is needed. These system elements

are as follows: a part that converts kinetic energy of a fluid to mechanical energy (consisting of a VIV cylinder with underwater housing), a part that converts linear translation motion to rotational reciprocal motion (consisting of a mechanical gear, coupling, and belt), and a part that converts rotational mechanical energy to electrical energy (the generator).

This paper focuses on the performance analysis and estimation of the electrical parameters of the Z hydrokinetic energy applications using analytical magnetic field calculations. Using a 2D polar coordinate system and a magnetic vector potential, the magnetic field solutions due to PMs and stator winding currents are derived. By using the derived magnetic field solutions and a 2D permeance function that takes into account skew effects, analytical expressions for electrical parameters such as the back-emf constant and air-gap inductance that also take skew effects into account are established. Then, on the basis of the estimated parameters and an equivalent circuit (EC), the output performances of the PMSG are investigated. All analytical results according to stator skews are shown to be in good agreement with the non-linear finite element (FE) calculations. In particular, measurements of the back-emf

*Corresponding author: Tel: +82-42-866-3873

Fax: +82-42-866-3819, e-mail: jschoe@moeri.re.kr

and inductance are presented to confirm the analyses. Finally, future directions for research on the hydrokinetic energy applications using VIV are discussed in terms of the evaluation of the system's performance and dynamic system modeling.

2. VIV Hydrokinetic Energy Converter with PMSG

2.1. System Configuration

Fig. 1 shows the schematic of the VIV hydrokinetic energy converter with PMSG. The electric power generation procedure of this system is as follows: (1) the mover in Fig. 1 begins to move upward or downward due to the velocity of running water in which it is submerged, (2) the mechanical power captured by the mover is transferred to the mechanical components indicated by circles (a and b in Fig. 1), which transform the linear translation motion into rotational reciprocal motion ($\pm \pi/4$ mechanical radian), and (3) the PMSG is driven by a belt connected to the mechanical components indicated by circles. It should be noted that four sets of mechanical springs are employed in order to utilize the mechanical resonance between the mechanical spring and the moving mass. Moreover, this system has the advantage that a wide range of running fluid velocities can be used, which makes the use of a mechanical resonance possible.

2.2. Configurations and Analytical Model of PMSG

Fig. 2 shows a schematic of the PMSG with a 20-pole PM rotor and a 24-slot skewed stator and photographs of these manufactured parts. The materials used for the magnet and stator core in this PMSG are NdFeB42 (its remanent flux density at 20°C is almost 1.3 T) and 50PN440 (the thickness of a laminated steel sheet is 0.5 mm), respectively. The stack length of the rotor and

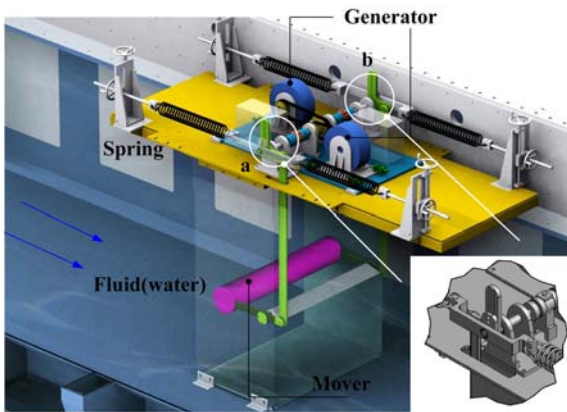


Fig. 1. (Color online) Schematic of the VIV hydrokinetic energy converter with PMSG.

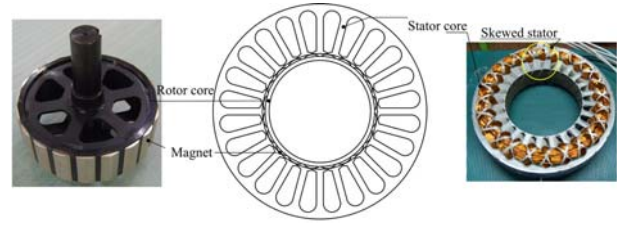


Fig. 2. (Color online) Schematic of the PMSG shown in Fig. 1 (center) and a photograph of its PM rotor (left) and skewed stator (right).

stator are 62 mm and 60 mm, respectively. The radius of the rotor core is 102 mm; the magnet thickness and air-gap length are 5 mm and 0.5 mm, respectively. As shown in Fig. 2, the magnets are machined to have a bread-loaf shape to generate a sinusoidal back-emf waveform. The weight of the rotor is minimized to reduce the rotary inertia due to the rotational reciprocal motion, and the stator is skewed by a half slot-pitch angle (7.5° in our model) to reduce the cogging torque.

Fig. 3 shows the simplified analytical model used for the prediction of magnetic field distributions produced by the PMs and the stator winding currents obtained from the following set of assumptions [3,4] First, the permeability of the stator and rotor yoke is infinite; second, the relative permeability of the PM is unity; finally, the current is distributed in an infinitesimally thin sheet at $r = R_s$. With these three assumptions, the analysis of the magnetic field due to PMs is confined to two regions referred to as the air (I) and magnet (II) regions, as shown in Fig. 3(a), whilst that due to stator currents is confined to only one region, as shown in Fig. 3(b). Here, R_i , R_o , and R_s represent the inner and outer radius of the PMs and the

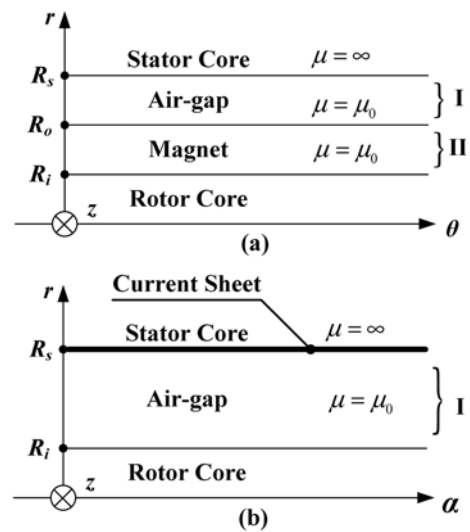


Fig. 3. Analytical model for the prediction of (a) open-circuit field and (b) armature reaction field.

inner radius of the stator, respectively. θ and α are the angular position of the rotor and the stator, respectively, which are related by $\theta = \alpha + \omega_r t$. ω_r is the rotational speed expressed in radians per second.

3. Problems in Formulas

3.1. Magnetic Fields produced by Permanent Magnets

Let us obtain the governing equations for open-circuit field analysis. In the magnet region, $\mathbf{B} = \mu_0(\mathbf{H} + \mathbf{M})$ and $\nabla \times \mathbf{H} = \mathbf{0}$ owing to the absence of free current in this region. Therefore, $\nabla \times \mathbf{B} = \mu_0 \nabla \times \mathbf{M}$. The magnetic vector potential \mathbf{A} is defined as $\nabla \times \mathbf{A} = \mathbf{B}$. Therefore, Laplace's and Poisson's equations in terms of the Coulomb gauge $\nabla \cdot \mathbf{A} = 0$ are given as follows: [5, 6]

$$\begin{aligned} \nabla^2 \mathbf{A}_{pm}^I &= 0 \\ \nabla^2 \mathbf{A}_{pm}^{II} &= -\mu_0(\nabla \times \mathbf{M}) \end{aligned} \quad (1)$$

where the subscript pm indicates a magnetic quantity generated by the PMs, μ_0 is the permeability of air, and \mathbf{M} is the magnetization of parallel magnetized PMs that are bread loaf shaped. This magnetization can be expressed as

$$\mathbf{M} = \frac{B_r}{\mu_0} \cos(p\theta) \mathbf{i}_z \quad (2)$$

where B_r and p are the remanent flux density of PMs and the number of pole-pairs, respectively. The vector potential has only the z or axial component, resulting in $\mathbf{A} = A_{pm}(r) \cos(p\theta) \mathbf{i}_z$. Therefore, the solution for Laplace's equation in (1) can be obtained as follows:

$$\mathbf{A}_{pm}^I = \{C_n^I r^p + D_n^I r^{-p}\} \cos(p\theta) \mathbf{i}_z \quad (3)$$

The solution for Poisson's equation in (1) can be also obtained as follows:

$$\mathbf{A}_{pm}^{II} = \left\{ C_n^{II} r^p + D_n^{II} r^{-p} - \frac{rpB_r}{\{1-(p)^2\}} \right\} \cos(p\theta) \mathbf{i}_z \quad (4)$$

In conclusion, by substituting (3) into the definition of the magnetic vector potential, namely, $\nabla \times \mathbf{A} = \mathbf{B}$, the normal (\mathbf{B}_{pm}^r) and tangential (\mathbf{B}_{pm}^θ) air-gap flux densities produced by the PMs can be obtained as follows.

$$\begin{aligned} \mathbf{B}_{pm}^r &= \frac{\partial}{\partial r} A_{pm}^I(r) \cos(p\theta) \mathbf{i}_r \\ \mathbf{B}_{pm}^\theta &= -\frac{\partial}{\partial r} A_{pm}^I(r) \sin(p\theta) \mathbf{i}_\theta \end{aligned} \quad (5)$$

The undefined coefficients C_n^I , C_n^{II} , D_n^I , and D_n^{II} can be determined easily by applying the proper boundary condi-

tions to (5).

3.2. Magnetic Fields produced by Stator Winding Currents

Fig. 4 shows the model for the Fourier series expansion of the current density for phase A of the PMSG shown in Fig. 2. Here b_o and t_o denote a slot opening width and a mechanical angle corresponding to the stator tooth width, respectively. $2N$ and i_a are the number of turns per slot and the current amplitude for phase A, respectively. The current density distribution of phase A can be expressed from Fig. 4 as follows:

$$\mathbf{J}_A = \sum_{n=1,odd}^{\infty} I_n i_a \cos(2n\alpha) \quad (6)$$

where I_n is the n^{th} -order Fourier series coefficient for the current density distribution for phase A and n is the n^{th} -order harmonic. Because 3-phase stator windings are wound $2\pi/3$ electrical radians apart in space, the Fourier series expansions for phase **b** and **c** are obtained as follows:

$$\mathbf{J}_B = \sum_{n=1,odd}^{\infty} I_n i_b \cos\left\{2n\left(\alpha - \frac{2\pi}{3}\right)\right\} \quad (7)$$

$$\mathbf{J}_C = \sum_{n=1,odd}^{\infty} I_n i_c \cos\left\{2n\left(\alpha - \frac{4\pi}{3}\right)\right\} \quad (8)$$

where i_b and i_c are the current amplitude for phase B and phase C, respectively. Through similar steps as in the PM case, the governing equation for the armature reaction field analysis produced by stator winding currents of phase A is obtained from Fig. 3(b) as follows:

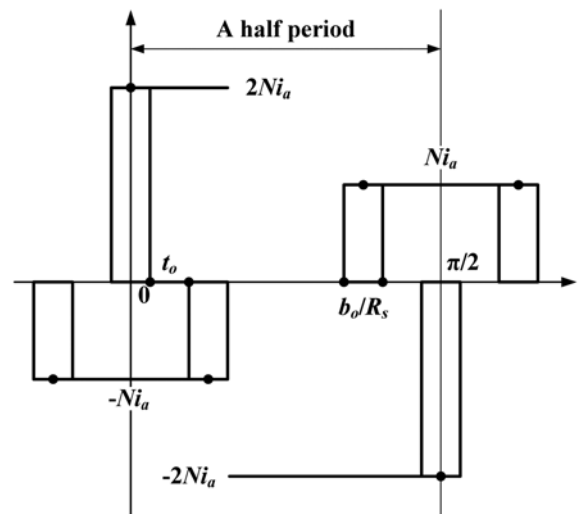


Fig. 4. Model for the Fourier series expansion of the stator current density.

$$\nabla^2 \mathbf{A}_{s_A}^I = 0 \quad (9)$$

where the subscript s_A represents a magnetic quantity generated by the stator currents of phase A. The vector potential (\mathbf{A}_{s_A}) also only has z or axial components and is expressed as follows.

$$\mathbf{A}_{s_A}^I = \sum_{n=1,odd}^{\infty} A_{s_A}^I(r) \cos(2n\alpha) \mathbf{i}_z \quad (10)$$

Therefore, the solution for Laplace's equation expressed in (9) can be obtained by substituting (10) into (9) as follows:

$$\mathbf{A}_{s_A}^I = \sum_{n=1,odd}^{\infty} \{E_n^I r^{2n} + F_n^I r^{-2n}\} \cos(2n\alpha) \mathbf{i}_z \quad (11)$$

By substituting (11) into $\nabla \times \mathbf{A} = \mathbf{B}$, the normal ($\mathbf{B}_{s_A}^r$) and tangential ($\mathbf{B}_{s_A}^\alpha$) air-gap flux densities produced by the stator currents of phase A can be also obtained as follows.

$$\mathbf{B}_{s_A}^r = \sum_{n=1,odd}^{\infty} \frac{2n}{r} A_{s_A}^I(r) \sin(2n\alpha) \mathbf{i}_r \quad (12)$$

The undefined coefficients E_n^I and F_n^I can be also easily determined by applying the proper boundary conditions to (12). On the other hand, because the current density \mathbf{J}_A is not included in (12) due to the current sheet assumption, this source term should be included in the boundary condition as $\mathbf{B}_{s_A}^\alpha(R_s, \alpha) = -\mu_0 \mathbf{J}_A$.

The flux density produced by the stator currents of phase B and C can also be calculated by methods used in the derivation of it due to current of phase A. However, as stated above, because 3-phase stator windings are wound $2\pi/3$ electrical radians apart in space, we can predict that the radial component of the flux density due to each phase is also separated by $2\pi/3$ electrical radians. As a consequence, the field produced by 3-phase windings in our model can be given as follows.

$$\begin{aligned} \mathbf{B}_s^r &= (\mathbf{B}_{s_A}^r + \mathbf{B}_{s_B}^r + \mathbf{B}_{s_C}^r) \\ &= \sum_{n=1,odd}^{\infty} \frac{2n}{r} A_{s_A}^I(r) \left[\sin(2n\alpha) + \frac{i_b}{i_a} \right. \\ &\quad \left. \sin\left\{2n\left(\alpha - \frac{2\pi}{3}\right)\right\} \frac{i_c}{i_a} \sin\left\{2n\left(\alpha - \frac{4\pi}{3}\right)\right\} \right] \mathbf{i}_r \\ \mathbf{B}_s^\alpha &= (\mathbf{B}_{s_A}^\alpha + \mathbf{B}_{s_B}^\alpha + \mathbf{B}_{s_C}^\alpha) \\ &= - \sum_{n=1,odd}^{\infty} \frac{\partial}{\partial r} A_{s_A}^I(r) \left[\cos(2n\alpha) + \frac{i_b}{i_a} \right. \\ &\quad \left. \cos\left\{2n\left(\alpha - \frac{2\pi}{3}\right)\right\} + \frac{i_c}{i_a} \cos\left\{2n\left(\alpha - \frac{4\pi}{3}\right)\right\} \right] \mathbf{i}_\theta \quad (13) \end{aligned}$$

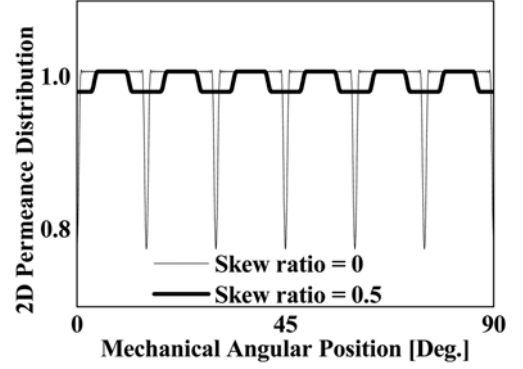


Fig. 5. 2D permeance distribution at $r = (R_s + R_o)/2$ at different stator skew ratios.

3.3. 2-D Permeance Function considering Stator Skew Effects

A 2-d permeance function is essential in order to consider slotting effects. Its analytical expression has already been established in Ref. 7. and is given as follows:

$$\lambda(r, \alpha) = \sum_{\mu=0,1,2,\dots}^{\infty} \Lambda_\mu(r) \cos \mu Q_s (\alpha + \alpha_{sa}) \quad (14)$$

where Q_s is the number of stator slots, and α_{sa} is determined by the winding pitch. $\Lambda_\mu(r)$ is also given fully in Ref. 7. Unfortunately, (14) cannot be applied to the PMSG with a skewed stator. However, a 2-d permeance function that takes into account skew effects can be obtained by applying a stator skew factor (S_n) to (14) as follows [8]:

$$\lambda^{skew}(r, \alpha) = \Lambda_0 + \sum_{\mu=1}^{\infty} S_n \Lambda_\mu(r) \cos \mu Q_s (\alpha + \alpha_{sa}) \quad (15)$$

where Λ_0 is the average value of the permeance for the case where $\mu = 0$ in (14). S_n is given as follows:

$$S_n = \frac{\sin(\mu Q_s \varepsilon / 2)}{\mu Q_s \varepsilon / 2} \quad (16)$$

where $\varepsilon = 2S_k \pi / Q_s$, S_k is the skew ratio.

Fig. 5 shows the 2D permeance distribution at a mechanical air-gap for different stator skew ratios, obtained from (15). It can be seen that the stator skew reduces the slotting effects of the stator. Expressions for the normal air-gap flux density due to PMs and stator winding currents that take into account slotting and skew effects can be written as follows.

$$\begin{aligned} \mathbf{B}_{pm}^{r(skew)} &= \mathbf{B}_{pm}^r(r, \theta) \lambda^{skew}(r, \alpha) \\ \mathbf{B}_s^{r(skew)} &= \mathbf{B}_s^r(r, \theta) \lambda^{skew}(r, \alpha) \quad (17) \end{aligned}$$

3.4. Back-emf Constant and Inductance

The back-emf voltage induced in the stator winding

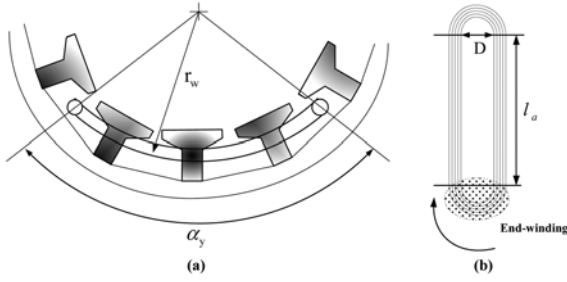


Fig. 6. Geometry for the calculation of the end-winding inductance.

coils due to magnet flux crossing the air gap is given by the rate of change in the flux linkage with respect to time as follows:

$$e_{back} = -\frac{d\Psi_{pm}}{dt} = -NN_c R_s l_a \Lambda_0 \frac{d}{dt} \int_{-\alpha_s/2}^{\alpha_s/2} \mathbf{B}_{pm}^r(R_s, \theta) d\alpha \quad (18)$$

where N_c is the number of coils per phase in the stator windings. δ_s and l_a are the stator winding pitch angle and the active stack length of the PMSG, respectively. Because (18) is not an analytical equation for back-emf that takes into account stator skew, \mathbf{B}_{pm}^r in (18) should be replaced by $\mathbf{B}_{pm}^{r(skew)}$ to account for the influence of the stator skew on the back-emf. However, this may cause analytical difficulties due to the complicated integrals in equation. Thus, we have chosen to use a skew factor for rotor magnets (R_n) in (18) using the fact that, analytically, rotor skew effects are the same as stator skew effects. As a consequence, the back-emf after skew effects are taken into account is given as follows.

$$e_{back}^{skew} = R_n e_{back} = \frac{\sin(np\varepsilon)}{np\varepsilon} e_{back} \quad (19)$$

The back-emf constant (k_e) can be easily obtained from (19) as follows.

$$k_e = \max(e_{back}^{skew}) / \omega_r \quad (20)$$

Through similar steps to those used in calculating the flux linkages due to PM, the flux due to the phase A currents linking the stator winding coils of phase A can be also calculated as follows:

$$\Psi_{s_A}^{skew} = NN_c R_s l_a \Lambda_0 S_n \int_{-\alpha_s/2}^{\alpha_s/2} \mathbf{B}_{s_A}(R_s, \alpha) d\alpha \quad (21)$$

The air-gap inductance (L_a) is obtained from (21) by $\Psi_{s_A}^{skew} = L_a i_a$. The self-inductance (L_{self}) is given by the sum of the air-gap inductance (L_a) and the end-winding inductance (L_{end}), which can be calculated as follows [9]:

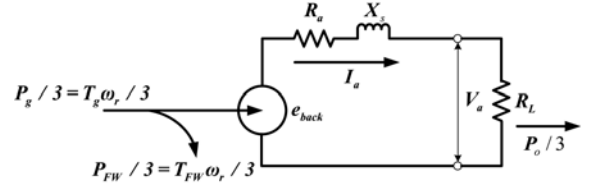


Fig. 7. Equivalent circuit for one phase of the PMSG

$$L_{emd} = \frac{\mu_0 p N N_c^2 D}{2 a_c^2} \log_e \left(\frac{4D}{GMD} - 2 \right) \quad (22)$$

where a_c is the number of parallel paths, respectively. GMD is the geometric mean distance between the conductors in the coil cross-section. As shown in Fig. 6, the end-windings are shaped in a circular arc. The diameter of the semicircular end-windings is $D = r_w \alpha_s$, and two such semicircles from opposite ends of the machine combine to make a complete circle.

If leakage inductance (L_{sl}) is neglected and the stator windings are balanced, the synchronous inductance (L_s) of a one-phase winding is given by the sum of the mutual inductance (M) and the winding's self inductance (L_{self}).

3.5. Equivalent Circuit

Fig. 7 depicts an equivalent circuit for one phase of the PMSG. Here, P_o , P_g , and P_{FW} are the output power of the PMSG, the input power of the PMSG, and the mechanical losses due to various causes such as bearing friction and windage loss, respectively. T_g and T_{FW} are the torques corresponding to the input power and mechanical losses. e_{back} , R_a , and X_s are the phase back emf, phase resistance, and phase reactance of the PMSG. Note that e_{back} is expressed as a peak value and X_s is given by $\omega_e L_s$. Here ω_e is given by $2\pi f_e$; f_e is an electrical frequency. From Fig. 7, the terminal voltage (V_a) and load current (I_a) of phase A can be obtained as follows.

$$I_a = \frac{e_{back}}{\sqrt{(R_L + R_a)^2 + X_s^2}} \quad (24a)$$

$$V_a = I_a R_L \quad (24b)$$

As a consequence, the output power (P_o) of PMSG can be obtained easily as follows:

$$P_o = (V_a I_a + V_b I_b + V_c I_c) \quad (25)$$

where the terminal voltage of phase B (V_b) and phase C (V_c) are given by $I_b R_L$ and $I_c R_L$, respectively, and the load current of phase B (I_b) and phase C (I_c) are given as follows.

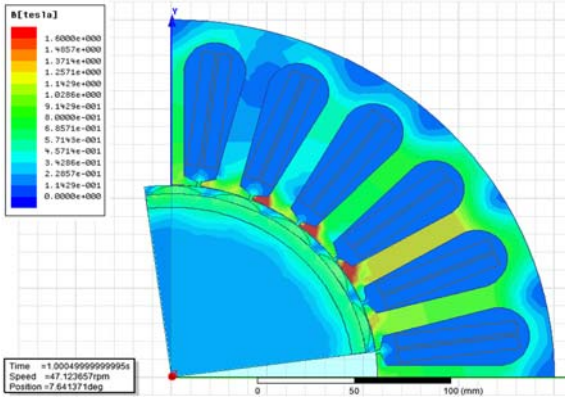


Fig. 8. (Color online) Flux density distribution produced by PMs, and obtained from 2D FE analyses.

$$I_b = I_a \frac{\sin(\omega_e t - 2\pi/3)}{\sin(\omega_e t)} \quad (26a)$$

$$I_c = I_a \frac{\sin(\omega_e t - 4\pi/3)}{\sin(\omega_e t)} \quad (26b)$$

4. Results and Discussion

4.1. Magnetic Fields produced by PMs and Stator Winding Currents

Fig. 8 shows the flux density distribution produced by PMs, which is obtained from 2D FE analyses. As shown in this figure, there is significant magnetic saturation in the teeth bottom regions, resulting in an increase of the cogging torque. However, it can be predicted that the cogging torque is reduced dramatically because of the skewed stator.

Fig. 9 shows the comparison of the analytical results with the non-linear FE calculations for the air-gap flux density produced by PMs for different stator skew ratios. The analytical results are shown to be in good agreement with the 2D FE results. These results confirm that the stator skew almost eliminates slotting effects.

Fig. 10 shows a comparison of analytical results and non-linear FE calculations for the air-gap flux density produced by stator winding currents of the PMSG with a skewed stator. The analytical results are also shown to be in good agreement with the 2D FE results. The air-gap flux density produced by the stator winding currents of the PMSG with a non-skewed stator is not presented because the influence of the stator slotting on the flux density is not significant.

4.2. Back-emf and Coil Inductances

Fig. 11 shows the comparison of analytical results and non-linear FE calculations for the back-emf at 50 rpm of

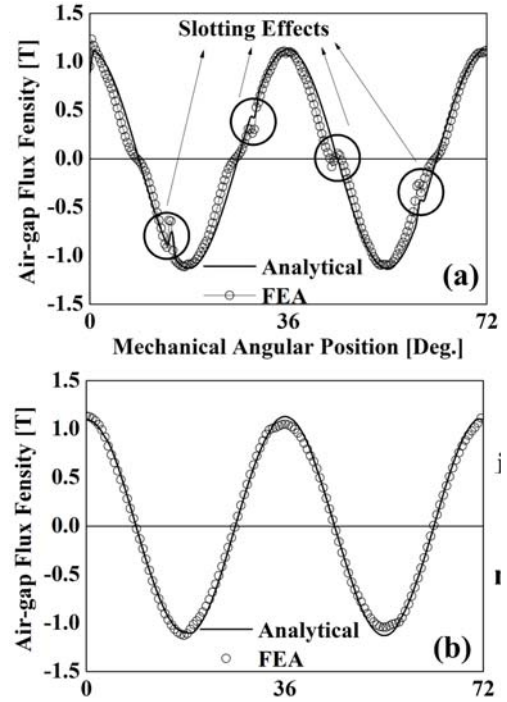


Fig. 9. Comparison of analytical results with non-linear FE calculations for the air-gap flux density produced by PMs for stator skew ratios of (a) $S_k = 0$ and (b) $S_k = 0.5$.

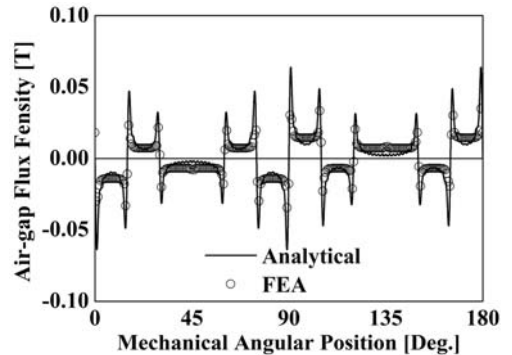


Fig. 10. Comparison of analytical results with non-linear FE calculations for the air-gap flux density produced by stator winding currents of the PMSG with a skewed stator.

the PMSG with and without a skewed stator. The analytical results are shown to be in good agreement with the 2D FE results. It can be observed that a stator skew makes the waveform of the back-emf more sinusoidal, while it reduces the back-emf amplitude. This is because a stator skew eliminates the harmonic components of the back-emf. It can also be observed that the back-emf constant for the PMSG with and without the skewed stator is 5.16 (V·s/rad) and 5.92 (V·s/rad), respectively.

Fig. 12 shows the line-line back-emf measurements of the PMSG with a skewed stator at 40 rpm. It can be seen

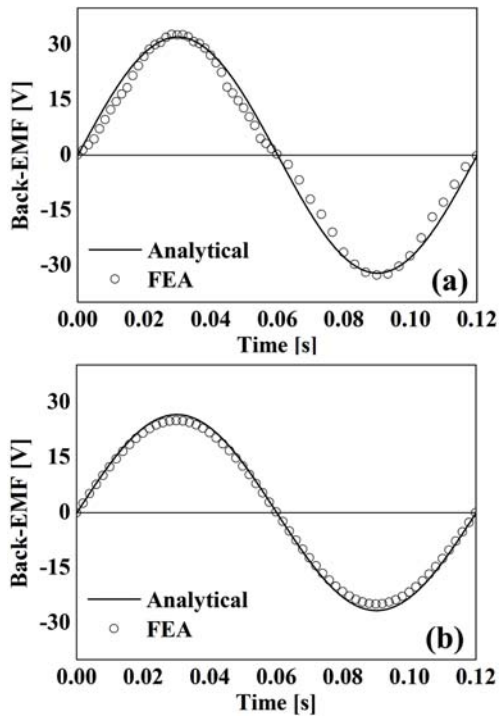


Fig. 11. Comparison of analytical results with non-linear FE calculations for the back-emf at 50 rpm for the case when the PMSG has (a) a non-skewed stator and (b) a skewed stator.

that the measured back-emf constant of the PMSG with the skewed stator is 5.3 (V·s/rad). This result confirms the validity of the magnetic field analysis produced by PMs that is presented in this paper.

Table 1. presents a comparison of the analytical results with measurements of the coil inductances. The measurements allow for an extensive validation of the analytical results. Therefore, this comparison confirms the validity of the magnetic field analysis produced by stator coil currents that is presented in this paper.

4.3. Generating Characteristics

Fig. 13 shows the variation of mechanical position and speed of the PMSG when the fluid velocity is 1 m/s. The mechanical position (θ_m) and speed (ω_m) of the PMSG can be expressed as follows.

$$\theta_m = \frac{\pi}{4} \sin(2\pi t) \quad (27a)$$

Table 1. Comparison of analytical results and measurements of the coil inductances.

		Analytical	Measurements
Self inductance	Air-gap inductance	12.8 mH	17.2 mH
	End-winding inductance	2.22 mH	

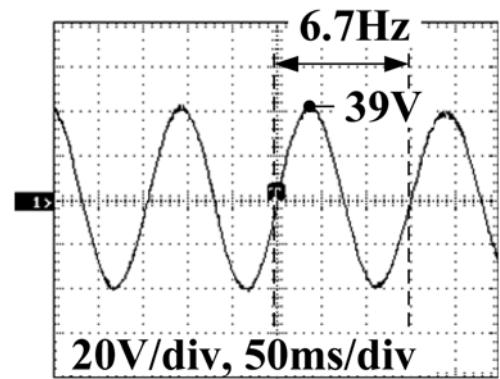


Fig. 12. Line to line back-emf measurements at 40 rpm.

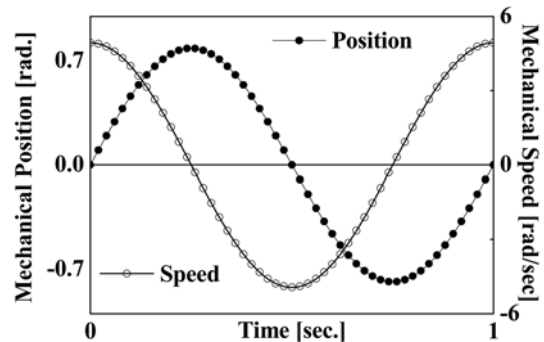


Fig. 13. Variation of mechanical position and speed of the PMSG when the fluid velocity is 1 m/s.

$$\omega_m = \frac{\pi^2}{2} \cos(2\pi t) \quad (27b)$$

By using (20) and (27b), the analytical expressions for the back-emf of the PMSG with rotational reciprocal motion can be given as follows:

$$e_{back}^{trans} = \omega_m k_e \sin(p \cdot \max(\omega_m) \cdot t) \quad (28)$$

To conclude, by replacing e_{back} in (24a) and ω_e in (26) with e_{back}^{trans} and $p \cdot \max(\omega_m)$, respectively, the output power of the PMSG with rotational reciprocal motion can be predicted from (25) analytically, as shown in Fig. 15. Fig. 15 shows the variation in the output power of the PMSG for various values of load resistance. The predictions are shown to be in good agreement with those obtained from non-linear FE analysis. Therefore, it can be judged that all analytical solutions presented in this paper are very useful for accurate and fast analysis of the PMSG for VIV hydrokinetic energy applications.

4.4. Future Work

This paper deals with the electromagnetic analysis of only the PMSG in VIV hydrokinetic energy converters. In order to implement a dynamic analysis of the PMSG for VIV hydrokinetic energy converters that takes into account

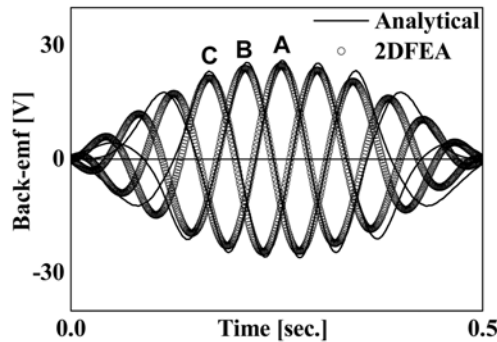


Fig. 14. Comparison of analytical results with non-linear FE calculations for the back-emf of the PMSG with the skewed stator at a fluid velocity of 1 m/s.

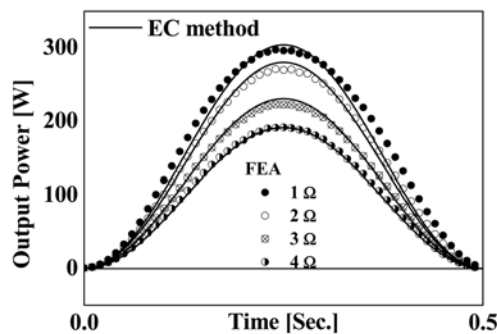


Fig. 15. Comparison of predictions with non-linear FEA for the output power of the PMSG with the skewed stator according to load resistance, for fixed values of rotor speed.

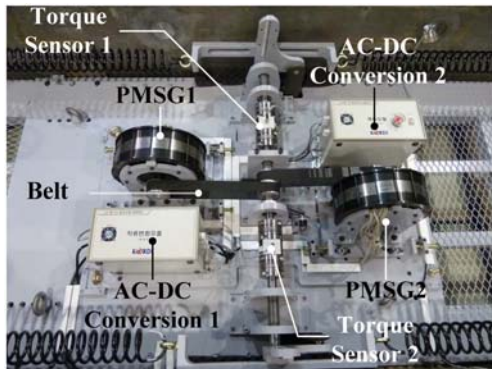


Fig. 16. (Color online) Experimental setup for the VIV hydrokinetic energy converter with PMSGs.

the parts involved in mechanical energy conversion (see Fig. 1), it is necessary to establish a dynamic simulation algorithm for the overall system. Therefore, in our future work, a dynamic analysis of the VIV hydrokinetic energy converters shown in Fig. 1 will be performed using analytical solutions for the circuit parameters of the PMSG presented in this paper. Moreover, the validity of the dynamic analysis will be confirmed through the

experimental system shown in Fig. 16, which shows the experimental setup for VIV hydrokinetic energy converters, and is constructed to be the same as the schematic presented in Fig. 1.

5. Conclusion

The analysis of the electromagnetic properties of the PMSG with a skewed stator for the VIV hydrokinetic energy applications has been described. Based on an analytical approach, magnetic fields due to PMs and stator winding currents, back-emf, and coil inductances that take into account the stator skew have been analyzed. Using estimated circuit parameters and simple EC methods, the output performances of the PMSG according to the load resistance have been also investigated. The FE and experimental results obtained from a developed PMSG with a skewed stator have confirmed the validity of the proposed analysis scheme. Back-emf and coil inductance measurements are presented to confirm the validity of the analytical calculations.

Acknowledgment

This work was supported by the New & Renewable Energy Technology Development Program of the Korea Institute of Energy Technology Evaluation and Planning (KETEP) grant funded by Korea government Ministry of Knowledge Economy (2009T100100321).

References

- [1] M. J. Khan, M. T. Iqbal, and J. E. Quicoe, *IET Renew. Power Gener.* **4**, 116 (2008).
- [2] R. D. Blevins, *Flow-Induced Vibration*, Krieger Publishing Company, Malabar (1990).
- [3] Z. Q. Zhu, D. Howe, and C. C. Chan, *IEEE Trans. Magn.* **38**, 229 (2002).
- [4] K. F. Rasmussen, In. *Proc. Int'l. Electrical Machines and Drives Conf.* **1**, 34 (1999).
- [5] D. L. Trumper, W.-j. Kim, and M. E. Williams, *IEEE Trans. IAS* **32**, 371 (1996).
- [6] J. Wang, G. W. Jewell, and D. Howe, *IEEE Trans. Magn.* **35**, 1986 (1999).
- [7] Z. Q. Zhu and D. Howe, *IEEE Trans. Magn.* **29**, 143 (1993).
- [8] K.-H. Kim, D.-J. Simm, and J.-S. Won, *IEEE Ind. Appl.* **1**, 191 (1991).
- [9] J. R. Hendershot Jr. and T. J. E. Miller, *Design of Brushless Permanent-Magnet Motors*, Oxford University Press, Oxford (1994).